Tsunami Deposits in a Super-large Wave Flume

3 authors, including:

Takumi Yoshii
Central research institute of electric power industry, Japan
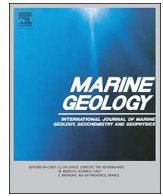**30** PUBLICATIONS   **169** CITATIONS

Masafumi Matsuyama
Central Research Institute of Electric Power Industry
83 PUBLICATIONS   **617** CITATIONS

CrossMark

Tsunami deposits in a super-large wave flume

Takumi Yoshii[a,*], Shiro Tanaka[b], Masafumi Matsuyama[c]

[a] River and Coastal Environment Sector, Environmental Science Research Laboratory, Central Research Institute of Electric Power Industry, 1646 Abiko, Abiko, Chiba 270-1194, Japan
[b] Geosphere Science Sector, Civil Engineering Research Laboratory, Central Research Institute of Electric Power Industry, 1646 Abiko, Abiko, Chiba 270-1194, Japan
[c] Planning and Administrative Team, Nuclear Risk Research Center, Central Research Institute of Electric Power Industry, 1646 Abiko, Abiko, Chiba 270-1194, Japan

ABSTRACT

Understanding the process of sediment transport under tsunami inundation is essential to providing credible information about potential tsunamis from tsunami deposits. In this study, a super-large wave flume 205 m long and 3.4 m wide was used to investigate the hydraulic process of tsunami inundation and sedimentary features of the resulting tsunami deposit. A uniformly sloping topography (1/50) with a sand dune 0.2 m high was built in the flume and the topography change induced by a solitary wave was measured. The maximum wave height at the shoreline was 0.6 m and the horizontal velocity reached up to 3.5 m/s, resulting in a sediment concentration of up to 5% by volume. The inundation and return flow completely eroded the dune and caused deposition, which showed landward and seaward thinning and fining. The vertical distribution of grain size and density in the inundation flow indicated upward fining and an upward decrease in density, and the deposits showed inverse grading at the base in addition to normal grading. Therefore, the inverse grading was attributed to the depositional process instead of the vertical distribution of grain size in the flow, such as via a traction carpet. The inundation flow was classified into two phases. The first phase flow, which appeared at the front of the inundation flow, was governed by the wave speed at the shoreline. The second phase flow, which occurred near the dune, was controlled by the difference in wave levels in front of and behind the dune. The deposits caused by the first phase flow (near the inundation limit) were constant regardless of the presence of the dune, indicating that the effect of the dune on the deposits was limited in the nearshore region. The deposits near the inundation limit, showing rapid fining and different chemical compositions, were carried by muddy foam floating on the water surface. The sediment supply from offshore to onshore over the dune was small and the erosion of the sand dune accounted for 36% of the onshore deposits. The offshore deposits were mainly caused by wave motion and the contribution of the onshore sediment brought by the return flow was small (24%). However, the return flow had a large effect on the sedimentary structure of the offshore deposits, such as seaward fining. Our results will help to examine the physical processes resulting in the empirically established common sedimentary characteristics of tsunami deposits and will provide a detailed data set to validate sediment transport models used in numerical simulations.

1. Introduction

Tsunami deposits, ranging from mud to huge boulders, are a fascinating tool for geology and seismology because they allow understanding of the history of ancient tsunamis over the past few thousand years. After several megathrust earthquakes and resulting catastrophic tsunamis in recent decades, information on ancient tsunamis has been growing in importance for engineering applications, including urban policy, evacuation planning, and nuclear hazard assessment (e.g. González et al., 2007; Japan Nuclear Energy Safety Organization, 2014).

The accumulation of geological information about tsunami deposits in the field, mainly since the 1990s, empirically revealed the characteristics of present (e.g. Peters and Jaffe, 2010) and ancient (e.g. Goff et al., 2010) tsunami deposits. The commonly observed characteristics are objective, reliable identification criteria for tsunami deposits (e.g. Chagué-Goff et al., 2011; Chagué-Goff et al., 2012b). Recent studies reconstructed the hydraulic parameters of tsunamis from tsunami deposits by using inverse analyses (e.g. Jaffe and Gelfenbaum, 2007; Soulsby et al., 2007; Furusato and Tanaka, 2014; Tang and Weiss, 2015).

Despite the progress in geological studies, hydrodynamic studies on

the processes of tsunami inundation, sediment transport, and deposition are still limited. Geological studies are usually conducted in places likely to preserve deposits, such as shallow lakes, marshes, and gently sloping topography. In particular, sand dunes near the shoreline are expected to be suitable places, mainly because of the undisturbed environments behind the dune and the ease of identification (e.g. Nanayama et al., 2003; Monecke et al., 2008; Prendergast et al., 2012). In these topographies, topography change, sediment transport, and deposition contribute greatly to the complexity of hydrodynamics behind dunes.

Experimental investigation is a promising method for unearthing sediment transport during tsunamis (Jaffe et al., 2016). However, laboratory experiments for tsunami sediment transport face problems with scaling. The settling velocity of particles can violate the theoretical scale ratio. The scaling rule based on the Froude number, which is commonly used for similarity criteria to scale down the hydraulic parameters, requires the settling velocity to follow the square root of the physical scale ratio. However, the settling velocity of particles < 62.5 μm is proportional to the square of grain size according Stokes' law, which violates the scaling rule.

Therefore, most experimental approaches to sand transport during tsunamis have increased the horizontal velocity instead of scaling down particle size (e.g. Takahashi et al., 2000; Yoshii et al., 2009; Yamaguchi and Sekiguchi, 2015; Johnson et al., 2016). These approaches have contributed to understanding the local sediment transport under high horizontal velocity. Because the topography from offshore to the inundation limit has not been reproduced in small-scale experiments, the source of tsunami deposits, erosion and deposition processes, and topography change remains unclear.

In this study, we tackled the scaling problem in laboratory experiments by using one of the largest wave flumes in the world. The Tsunami Sand Transport Laboratory Experiment (TSTLE) project was launched in the Central Research Institute of Electric Power Industry (CRIEPI) to study hydrodynamics of tsunami inundation, sediment transport, and consequent deposits at a high Shields number. This enormous flume enabled us to reproduce the topography from offshore to the inundation limit with a reasonable land slope of 1/50. We focused on the inundation process, sediment transport, and deposition on topography with a sand dune.

2. Methods

We conducted laboratory experiments with a super-large wave flume at CRIEPI (CLWF) (Fig. 1). In the movable-bed channel, a sand bed covered the floor from the start of the channel to 10 m behind the shoreline. A sand dune (0.2 m height, 0.2 m crest width, 0.8 m total width) was located 0.4 m behind the shoreline. The grain size distribution of the sand had a bimodal distribution with peaks at 0.2 and
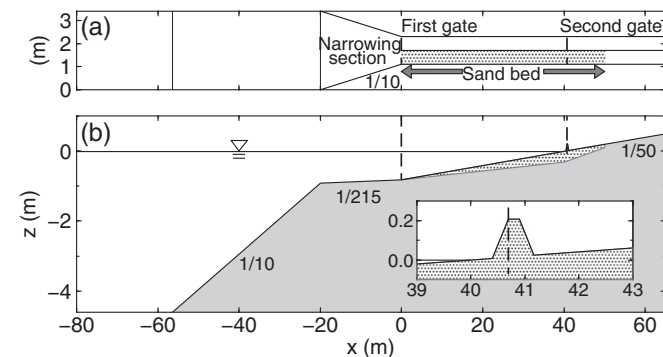
Fig. 2. Grain size distribution of the bed material.

Table 1
Conditions for experimental cases.

Case	Waveform	Dune	Overflow	2nd gate	Trap
C1	Bore	×	×	×	×
C2	Bore	✓	×	×	×
C3	Peaked	✓	✓	×	×
C4	Peaked	✓	✓	✓	×
C5	Peaked	✓	✓	×	✓

1–2 mm (Fig. 2). The sand consisted of iron sand (D50 ≈ 0.12 mm) and a small amount of silt and mud (1.3%). Although the sand was silica-dominant, it contained Al_2O_3 (10.9%) and Fe_2O_3 (7.3%).

We examined five experimental cases with different wave parameters, topography, and gate operation (Table 1). The bore waves (C1 and C2) did not overflow at the end of the channel, whereas the peaked wave (C3–C5) overflowed at the end (Fig. 3). Turbidity (x = 36 and 44 m) and water level (x = 40 and 50 m) were measured in the movable-bed channel, whereas the velocity and water level were measured in the fixed-bed channel. The return flow was blocked by the second gate in C4. The vertical distribution of sediment transport was measured by using the sediment trap in C5.

We obtained sediment samples before and after the experiments and measured the chemical composition and grain size. Hereafter, the weight fraction of grains of ≥ 1 mm is referred to as D_{vcs} and the median diameter of grains with < 1 mm is referred to as D50.

The model setup, experiments, and analysis are described in full in Supplementary information A.

3. Results

3.1. Hydrodynamics of tsunami inundation

3.1.1. Inundation flow and return flow

The wave collapsed offshore and changed into a bore waveform at the shoreline, and then inundated landward causing a high horizontal velocity at the front of the bore (a detailed description is given in Supplementary information B.1). The wave speed increased as it

Fig. 1. (a) Plan view and (b) section view of the experimental model. The inset in (b) shows a magnified portion of the section view. The x-axis is defined in the landward direction from the entrance of the channels and the z-axis is defined in the vertical direction from the water surface. The sand bed is set in the dotted area.
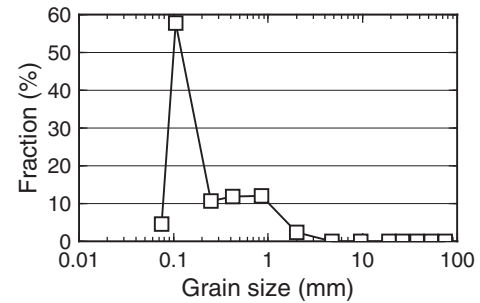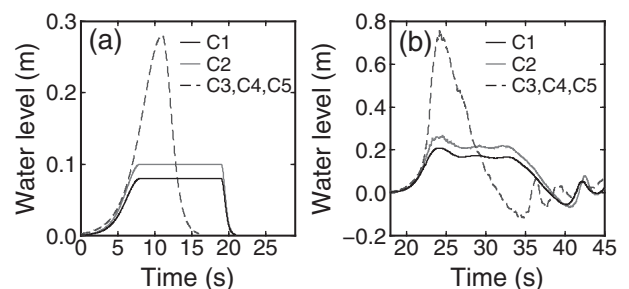
Fig. 3. (a) Input waves for the wave generator and (b) the progressing waves observed at x = 0.5 m.
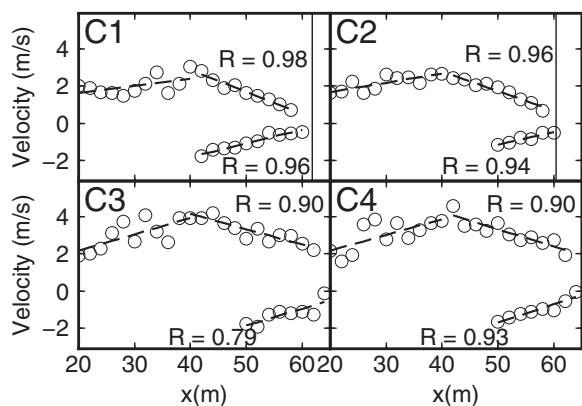
Fig. 4. Wave speed and maximum velocity of the inundation flow and return flow. The maximum velocity of the inundation flow was calculated from the water level. The velocity near the dune was excluded from the approximation. $x \leq 41$ m for the inundation flow, $x < 50$ m for the return flow in C2, C3, and C4. The broken lines show the approximations.

approached the shore and reached 2.6–2.7 m/s (C1, C2) or 3.8–3.9 m/s (C3, C4) (Fig. 4). The inundation speed was consistent with the wave speed at the shoreline and decreased with the distance from the shoreline. The gradient of the approximated lines in C1 and C2 (-0.11 to -0.12 /s) was larger than that in C3 and C4 (-0.08 to -0.09 /s). The return flow increased with the distance from the inundation limit or the end of the channel and became a supercritical flow. The slope of the approximated lines was 0.08–0.10 (/s), and there was no significant difference between experimental cases.

We compared the deceleration of the inundation flow with the gravity component parallel to the slope ($g \cdot \sin\theta$). The deceleration in C1 and C2 corresponded to that attributed to the gravitational effect. However, the deceleration in experimental cases with larger waves (C3 and C4) was slightly larger than that expected from the gravitational effect (ratios of 1.3–1.5).

3.1.2. Flow around the dune

When the dune caused the superposition of the reflected wave on the incoming wave, the water level in front of the dune increased rapidly (Supplementary information B.1). The large difference in water level in front of and behind the dune induced a strong, steady landward current behind the dune. The Froude number of this flow was stable at 1.65 (C2) and 1.72 (C3), except for the initial phase of the inundation flow with an instantaneous strong current (Fig. 5). The flow volume calculated by using Honma's formula (Honma, 1940) corresponded well to the observed flow in C2 and C3, except during the initial inundation.
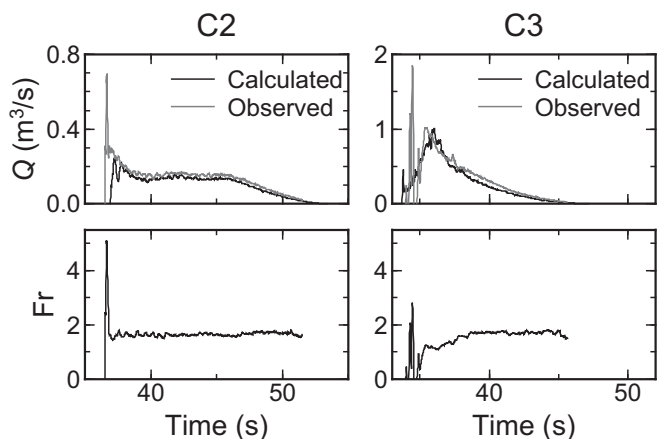

Fig. 5. Flow volume (Q) and Froude number (Fr) behind the dune ($x = 40.9$ m). The flow volume calculated by Honma's formula is also showed in figures.
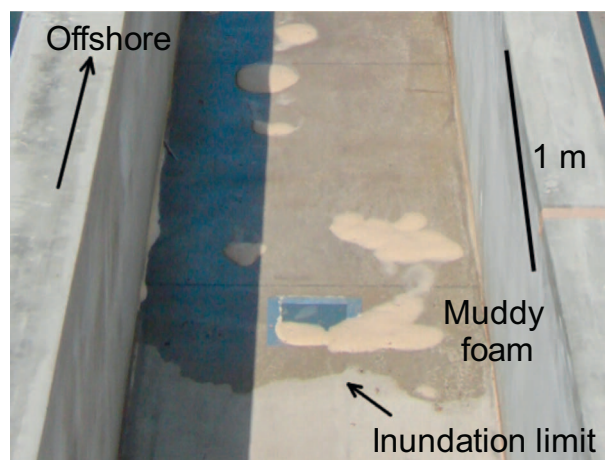

Fig. 6. Photograph of the inundation limit just after the experiment (C2).

This result indicated that the flow behind the dune was controlled by the water level in front of the dune and the shape of the dune.

3.2. Sediment transport and deposition

The inundation flow produced suspended sediment and many muddy bubbles around the shoreline or behind the dune (see video images in Appendix A). The Shields number of the inundation flow was estimated to have reached 8 for the peak waves (C3, C4) and 4 for the bore waves (C1, C2) at the front of the wave (a detailed description is given in Supplementary information B.3). The turbidity at $x = 44$ m increased rapidly to 15% at the front of the inundation flow in all experimental cases. The floating bubbles were brought to the inundation limit by the inundation flow in C1 and C2. Most of the bubbles were carried back offshore by the return flow, except near the limit where the muddy foam remained (approximately $x > 58$ m) (Fig. 6).

The time-stack images (Fig. 7) also showed the dense sediment transport at the front of the inundation flow (video images also

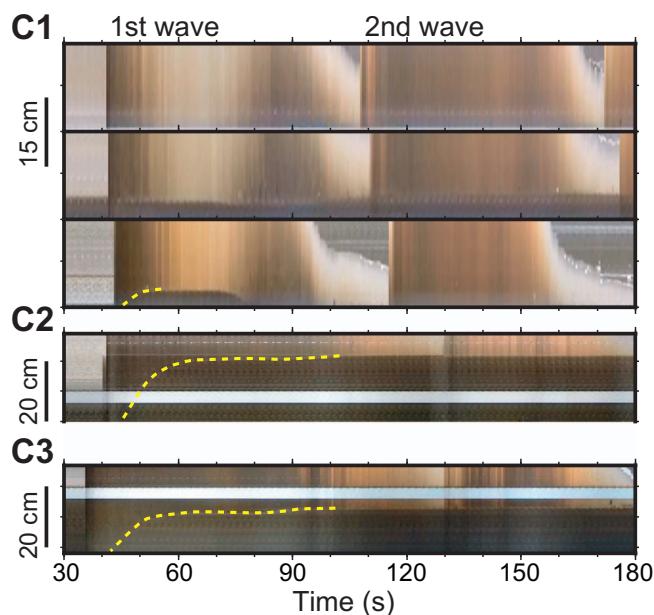**Fig. 7.** Time-stack images of the side view recorded at (C1) $x =$ (top) 41.5, (middle) 42.5, and (bottom) 44 m, and at (C2, C3) $x = 42.5$ m. A stain on the acrylic is visible as a gray area in C1 at $z < 5$ cm and $x = 42.5$ m. The broken lines indicate the surface of the bed and the top of the white bands in C2 and C3 shows the original bed surface. A mound appears at $t = 45$–70 s at $x = 44$ m in C1 showing topography change.
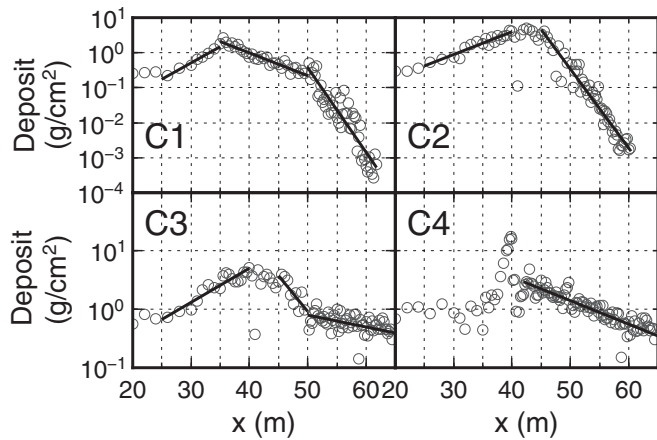
Fig. 8. Amount of deposits and approximation lines.

available in Appendix A). The image at x = 44 m in C1 showed that dense landward sediment transport caused the deposition with height of 4 cm deposition at t = 46–49 s, and that the return flow eroded this deposition completely at t = 74–79 s. In experiments with the dune, major erosion of more than 10 cm (C2) and 20 cm (C3) occurred in the first 3–4 s of the inundation flow. Rapid, significant deposition occurred at 10–15 s, and then the deposition became gradual.

3.3. Spatial distribution of deposits

The dune was completely eroded and the topography became nearly flat (see Supplementary information B.4 for further explanation). The cross-shore distribution of the amount of deposits showed landward and seaward thinning (Fig. 8). The spatial distribution of the amount of deposits was represented well by exponential curves (R > 0.92). The slope in the nearshore region in C2 was larger than that in C1; however, the amount of deposits and the deposit distribution at x ≥ 50 m in C2 were similar to those in C1, despite the presence of the dune. The grain size distribution also showed landward and seaward fining. The deposits near the inundation limit showed a rapid change in grain size and chemical composition and we confirmed that this change was caused by the increase of iron sand, mica flakes, and clay minerals in the deposits (Fig. 9). Although the experiments without the return flow produced offshore deposits (Fig. 10), the offshore thinning and fining was not significant.

The total amount of deposits in C2 was larger than that in C1, and the difference was larger than the size of the dune (Fig. 10). The scouring behind the dune in C2 increased the onshore erosion, which accounted for 18% of the total amount of deposits. The ratios of the amount of erosion and deposition in the offshore region to those in the
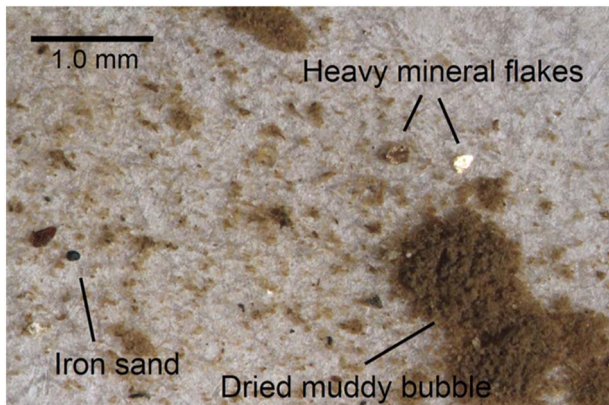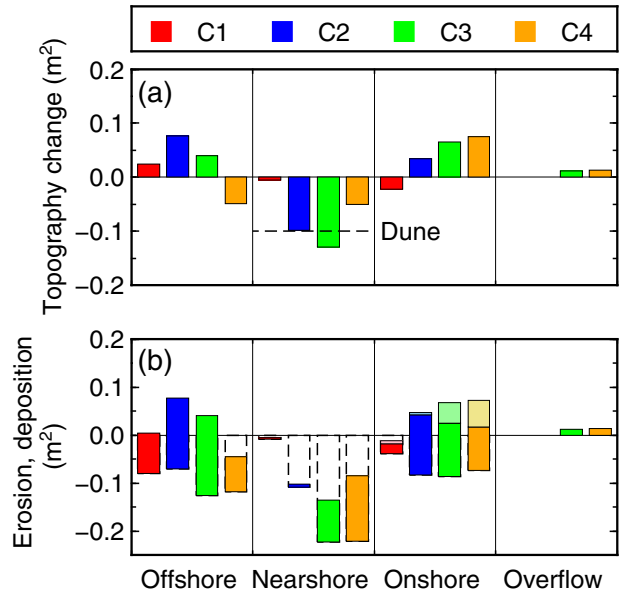

Fig. 10. (a) Total amount of topography change and (b) amount of erosion and deposition. The offshore, nearshore, and onshore areas correspond to x = 0–40.3, x = 40.3–41, and x = 41–65 m, respectively. The offshore area in C3 and C4 is x = 0–38.0 m to avoid the area being affected by gate operation. The lighter shading indicates the amount of sediment on the fixed bed.

onshore region in C1 were 2.0 and 3.9, respectively, indicating that the waves eroded the onshore region. In contrast, the ratios of erosion and deposition in C2 were 0.86 (erosion) and 1.2 (deposition). Therefore, the dune contributed to the uniform distribution of erosion and deposition.

3.4. Source of deposits

The onshore deposits came from the onshore erosion (64%) and the dune (36%), indicating that the sediment supply from the offshore region was small (Fig. 11). The inundation flow eroded 46% of the dune, whereas the rest of the dune was eroded by the return flow and brought offshore. The offshore deposits in C3 arose from offshore erosion (44%), the dune (32%), and the onshore region (24%). Because the onshore sediment contained the sediment supplied from the dune (36%), the proportion of sediment that originated in the onshore region in the offshore deposits was less than this estimate (24%).

3.5. Vertical distribution of suspended sediment

The vertical distribution of the amount of sediment caught in the

Fig. 9. Microphotograph of deposits near the inundation limit in C1 (x = 61.75 m).
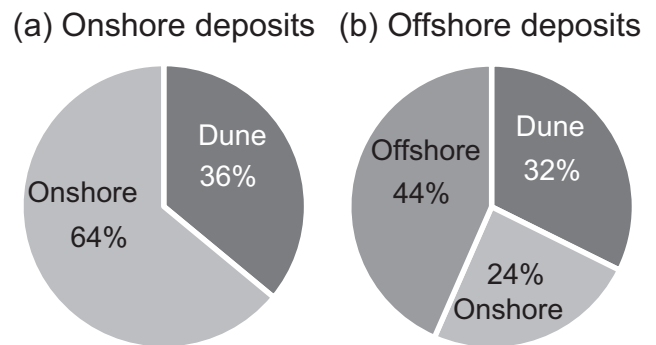
(a) Onshore deposits   (b) Offshore deposits

Fig. 11. Source of (a) onshore deposits and (b) offshore deposits. The offshore and nearshore regions were defined as x = 0–38.0 and 38.0–41.0 m, respectively, to avoid the area affected by the water leakage.
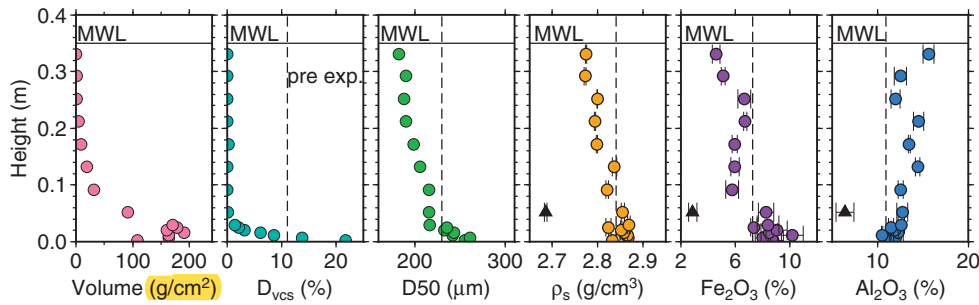
Fig. 12. Vertical distributions of sediment volume, grain size, density, and chemical composition of the landward sediment transport at x = 51.0 m. The broken lines indicate the initial value of the bed. The black triangles in the density and chemical composition distributions show the values for grains of > 1 mm. The standard error is indicated by horizontal lines.

trap showed an upward decrease except for the upward increase near the bed (Fig. 12). The amount of sediment from the bottom to a height of 0.09 m was more than 90% of the total sediment volume, and the amount up to a height of 0.21 m was more than 99%. The grain size distribution showed clear upward fining for D_{vcs} and D50. D_{vcs} values for the two traps from the bottom were 21.8% and 13.7% and the fraction rapidly decreased to < 1% at a height of 0.05 m. In contrast, the vertical distribution of D50 showed nearly uniform upward fining, except for rapid fining near the bottom. The grain density and Fe_2O_3 content showed an upward decrease, whereas the Al_2O_3 content showed upward increase and reached 16%.

3.6. Sedimentary structures of the deposits

The deposits on the fixed-bed section in C4 showed clear inverse grading near the bed and normal grading in the upper part (Fig. 13 (a)). The fraction of coarse sand was small near the bottom and reached its maximum at 4.5 mm from the bed. Similarly, D50 reached its maximum 1.3 mm from the bed and gradually decreased upward. The Fe_2O_3 content showed an upward decrease and the Al_2O_3 content showed an upward increase near the surface of the deposits. These characteristics were also observed in the deposits obtained at x = 50.25 and 52.25 m, although the maximum D50 was at a slightly different height (up to 5 mm) and the maximum D_{vcs} was higher (up to 40%).

In contrast to the measurements, the vertical distribution of the deposit, calculated from the vertical distribution of the suspended sediment, showed normal grading throughout the deposit (Fig. 13 (b)). The greatest difference between the distributions was that D_{vcs} in the

calculated deposit was concentrated near the bed and disappeared at a height of 1.5 mm. Correspondingly, the calculated maximum D50 value was smaller than the measured value and showed normal grading, except the near the bed. The Fe_2O_3 content reached a maximum near a height of 1.5 mm above the bed, which corresponded to the height where the coarse sand disappeared, and showed a uniform upward decrease. This result was different from the measurement results, which showed an iron-dominant layer on the bed.

3.7. Sediment concentration in the inundation flow

The time-averaged sediment concentration showed a landward decrease (Fig. 14). The concentration obtained from the deposits in C2, C3, and C4 reached 12–14% and decreased rapidly at x < 44 m. The concentration at x = 44 m in C2 was comparable to those in the experiments with the larger wave, although the velocity was smaller than those in C3 and C4. However, the concentration obtained from the turbidity at x = 44 m in C1 was 46% of that in C2.

3.8. Offshore sediment transport by return flow

The amount of sediment return to offshore at x = 51 m in C3 was calculated to be 8.6–17.7% of the sediment in the inundation flow. The proportions of sediment in the return flow to sediment in the inundation flow at x = 44 m were calculated to be 28% (C1), 23% (C2), 9% (C3), and 2% (C4). The flow volumes of the return flow measured in the fixed-bed channel in C2 and C3 were smaller than those in the movable-bed channel, because the dune was completely eroded by return current. However, the proportion at x = 44 m in C2 and C3 was consistent with the difference in the time-averaged concentration of inundation flow estimated from the turbidity and the amount of sediment (21% in C2, 10% in C3). This result indicated that a considerable part of the dune was not eroded by the landward inundation flow, which was consistent with 54% of the dune being eroded by the return flow (see
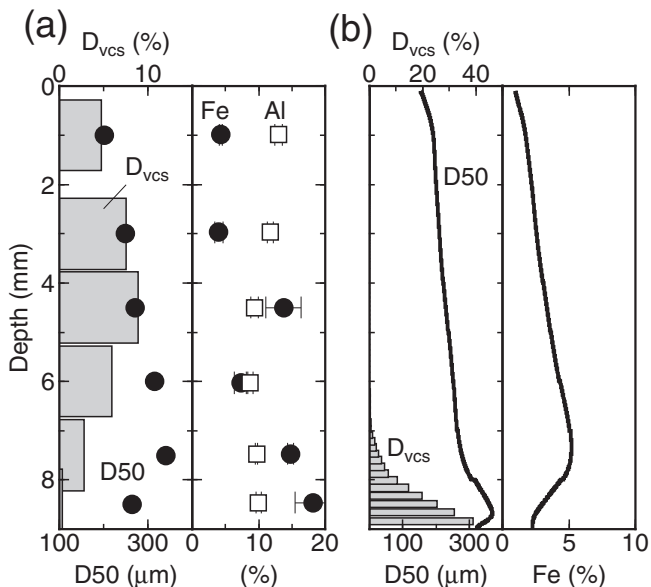
Fig. 13. Vertical distribution of D50, D_{vcs}, Fe_2O_3, and Al_2O_3 of (a) the deposits measured at x = 51.25 m in C4 and (b) calculated from the sediment trap results.
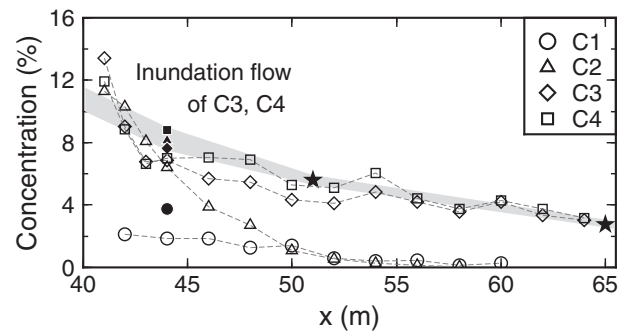
Fig. 14. Time-averaged sediment concentration in the landward inundation flow. The points were estimated from the amount of deposits and neglected the effect of the return flow. The star at x = 65 m indicates the concentration estimated by the overflow sediment in C3 and C4. The vertical bar at x = 51 m shows the concentration estimated from the amount of sediment in the sediment trap. The filled symbols at x = 44 m are the concentration estimated by using turbidity measurements.

Section 3.4). The proportion in C3 was smaller than the estimate obtained from the amount of topography change (24%), indicating the majority of the offshore sediment supply from the onshore region originated behind the dune.

4. Discussion

4.1. Inundation process of a tsunami on topography with a dune

4.1.1. Inundation flow

The inundation process of a tsunami over a sand dune consisted of two different phases: the initial phase appeared at the front of the inundation flow with an instantaneous strong current and the second phase appeared near the dune with a steady current. In contrast, the inundation on a uniform s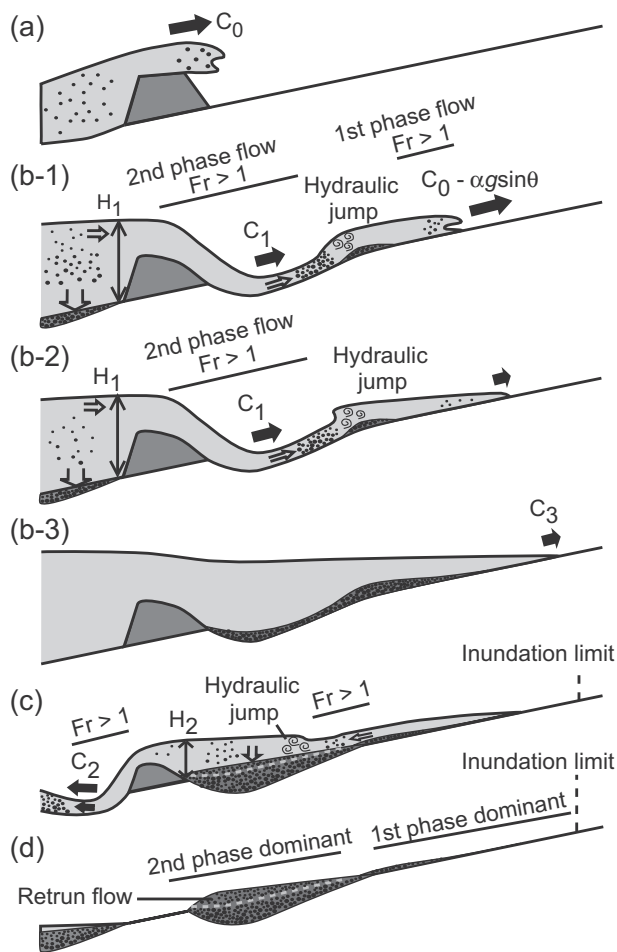loping plane topography only showed the initial phase. The flow in the initial phase was determined from the launch of the water mass from the shoreline (Fig. 15 (a)). This flow is referred to as the initial phase flow. The initial phase flow at the shoreline had similar velocity to the wave speed and the deceleration of the current depended on the land slope (Fig. 4). These results indicated that the inundation process of the first phase flow was governed by the law of conservation of momentum. Therefore, the maximum inundation height (distance) was determined by the wave speed at the shoreline, as shown by shallow-water theory (Shen and Meyer, 1963).

The effect of the dune on the first phase flow was small (< 22%, see Supplementary information B.1). Because the response angle of natural sand ranges from 30° to 40°, the rate of decrease ranges from 13% to 23%. Thus, the dune did not severely affect the first phase flow when the incident wave height was not considerably smaller than the dune.

The flow in the second phase, referred to as the second phase flow, was determined from the difference in the water levels in front of and behind the dune (Fig. 15 (b-1)). There was no major current in front of the dune because of the superposition of the incident wave and the reflection wave from the dune. Thus, the energy of the inundation flow was only supplied from the potential energy of the water in front of the dune. Consequently, the second phase flow could not reach an inland elevation higher than the water level in front of the dune (H_1 in Fig. 15). Because the second phase flow was a supercritical flow and usually accompanied by a hydraulic jump at the end of the flow, the extent of this flow was expected to be smaller than that predicted from its potential energy.

These inundation processes were hydrodynamically reasonable. However, for interpreting the deposits, it was important that the second phase flow was not directly related to the first phase flow (for detailed discussion, see Section 4.3). Because the first and second phase flows remained supercritical until they stopped, hydraulic information about the first phase flow did not propagate seaward beyond this supercritical flow (Fig. 15 (b-1)). Conversely, hydraulic information about the second phase flow did not reach the first phase flow. Thus, the inundation flow was divided into the second phase flow region, the first phase flow region, and the transition region depending on the dominant hydraulic parameters.

4.1.2. Inundation limit

The experiments indicated that the inundation limit is determined by the initial phase flow because the waveform leans forward with decreasing water depth (Fig. 15 (b-1)). If the wave is large and long enough to create a second phase flow that overtakes the maximum inundation distance of the initial phase, the inundation limit moves landward again (Fig. 15 (b-2)). In particular, if the wave does not create a large initial phase flow, the inundation limit is determined by the second phase flow. If the wave level continues to increase after the second phase flow reaches its potential maximum height, the water surface becomes nearly flat and the inundation limit moves landward, reflecting the increase of depth (Fig. 15 (b-3)). In this case, however, the horizontal velocity is much smaller than that caused by the first inundation processes because the horizontal velocity depends on the volume of water pooled behind the dune. The volume of water behind the dune is much larger than the water supply from offshore, resulting in the slow movement of the inundation limit and less sediment transport. Therefore, the first and second phase flows are the dominant processes in sediment transport and sedimentation.

4.1.3. Return flow

The maximum velocity of the return flow is assumed to be determined by the land slope and the wave surface slope. If the initial phase flow decides the inundation limit, then the slope of the water surface is consistent with the land slope. Therefore, the return flow is determined only by the land slope and the distance from the inundation limit, as observed in the experiments (Fig. 4). This uncomplicated relationship allows us to evaluate the magnitude of return flow and its effect on the deposits in the field.

The pseudo second wave induced by the return flow was important for interpreting the deposits. The return flow on a land slope of 1/50 became supercritical and made the hydraulic jump where it stopped (Fig. 15 (c)). The hydraulic jump behaves like the breaking waves, propagating shoreward with strong turbulence, especially in the nearshore region. Because this turbulence causes a large amount of sediment suspension (see Supplementary information B.3), the wave motion can produce an additional sedimentary structure on the deposits, which can confound the interpretation of inundation cycles. Therefore, it is important to assess whether the return flow at the measurement points can become supercritical.
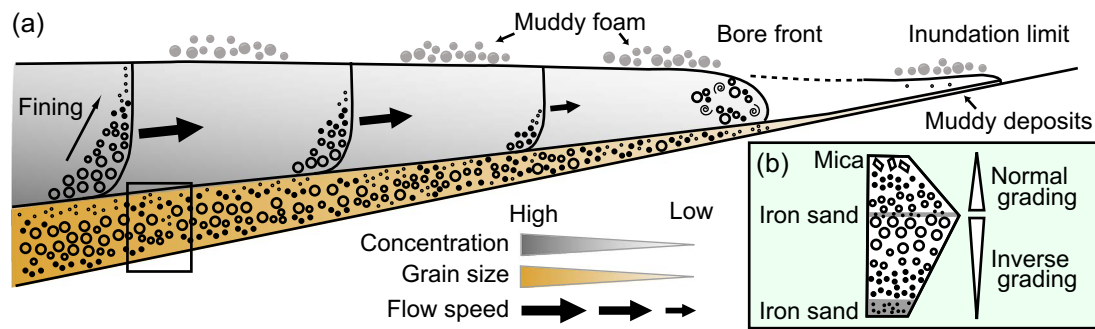
Fig. 16. Schematics of sediment transport and deposition under tsunami inundation. The inset in (b) shows the sedimentary structure of the deposits indicated by the rectangle in (a).

4.2. Sediment transport and deposits

4.2.1. Reproducibility of sediment transport

Large-scale experiments enabled us to reproduce the sedimentary structure of deposits. The flow with a very high Shields number, which was similar to that in actual tsunamis, caused dense sediment flow. The spatial distribution of the resulting deposits was similar to those observed in the field, showing landward thinning and fining (e.g. Peters and Jaffe, 2010) and muddy deposits near the inundation limit (e.g. Chagué-Goff et al., 2012a). Furthermore, the deposits showed normal grading and inverse grading, which are also typical characteristics of tsunami deposits (e.g. Peters and Jaffe, 2010). In addition, our ongoing research is revealing that the deposits mostly consist of two subunits, and that the top of the deposits is covered by finer materials (partly observed in Fig. 13). Thus, the deposits in this study had almost all the sedimentary characteristics observed in the field, except for rip-up clasts and loading structures, the formation of which depends on the underlying substrate.

Considering these similarities in hydraulic parameters and sedimentary characteristics, our experiments reproduced the sediment transport and the process of formation of deposits during tsunamis. The reproducibility of sediment transport in laboratory experiments has not been fully discussed although it is important for discussing the experimental results. Because small-scale laboratory experiments reproduce only a part of the tsunami propagation or inundation, these experiments lack information about sedimentary characteristics required for judging whether the reproducibility is sufficient. For example, some small-scale laboratory experiments have already reproduced the spatial deposition distribution (e.g. Harada et al., 2011; Johnson et al., 2016); however, the sedimentary structure of the deposits was not investigated, probably because they were not thick enough for observation. The hydraulic parameters measured in the present experiments could serve as standard values to produce the sediment transport of tsunamis in laboratory experiments because these parameters were confirmed to reproduce sand transport similar to that in the field.

4.2.2. Maximum sediment concentration

The upper threshold of sediment concentration is a critical parameter in the numerical simulation of tsunami sediment transport and strongly affects the result. In the present experiments, the concentration instantly reached 15% (5.3% by volume). The time-averaged sediment concentration behind the dune was estimated to be 11–13% (3.9–4.6% by volume). These concentrations were near the upper threshold of suspended sediment used in 2D numerical simulations (5% by volume) (e.g. Yoshii et al., 2011). Some numerical studies (e.g. Gusman et al., 2012; Sugawara et al., 2014) used a lower sediment concentration as the threshold value. Although the estimation method differs, Goto et al. (2014) reported that the average concentration in Sendai Plain is 2% (5% at 90% maximum) from the vast amounts of measurements. Our experiments illustrated that the sediment concentration was not saturated up to 15% (5.3% by volume) at least. Thus, a threshold of < 5% should not be used for sandy sediment.

4.2.3. Onshore tsunami deposits

The sand dune near the shoreline was the sediment source and created many deposits compared with the uniform sloping beach with no dune (Fig. 10). Thus, sand dunes should help the field investigation of tsunami deposits through providing an environment for preserving deposits and the easily recognizable thickness of the deposits. However, because the sediment supplied by the dune could not reach beyond the extent of the second phase flow, the dune did not increase the thickness of deposits near the inundation limit. Therefore, the advantages of investigating the deposits for the topography with the dune were limited to the nearshore region.

Furthermore, the rapid change in grain size and chemical composition of deposits near the inundation limit indicated that the dominant sediment transport mechanisms changed from the suspended and bed load mechanism to the floating load mechanism near the inundation limit (Fig. 16). We could not evaluate the quantitative effect of foam on the resulting deposits because the formation and transportation of muddy foam do not follow the scaling laws. However, the floating load may be dominant near the inundation limit in the field; some field investigations have reported that the constituents of deposits change from sandy to muddy near the inundation limit (e.g. Chagué-Goff et al., 2012a). In contrast to the suspended and bed loads, the floating load was not affected by flow speed and volume once foam formed on the surface. Thus, the floating load can transport sediment and form deposits far inland even by the shallow and slow inundation flow near the limit.

Understanding the effect of the floating load on deposits near the inundation limit in the field is important for discussing controversy around the extent of tsunami deposits and the inundation limit. Because we can only investigate the extent of ancient tsunami deposits, we need to relate the extent of deposits to the inundation limit. Thus, the seismic scale estimated from tsunami deposits increases when we assume there is a difference between deposits (e.g. Namegaya and Satake, 2014). It is important to investigate how much sediment floating load can carry and how large materials can be entrained in foam in the field. Considering the sediment density affects the suspension, some quite large particles with low density (e.g. pumice and coral) may float and move inland.

4.2.4. Vertical distributions of grain size and chemical composition

The landward and seaward fining were attributed to the difference in settling velocity because the vertical distribution of the grain size and density showed an upward decrease (Fig. 16). This mechanism of spatial distribution arises from particles with higher settling velocity accumulating faster than those with lower settling velocity because particles with high settling velocity are more concentrated near the bed. Because the vertical distribution of grain size depends on the shear velocity, the spatial distribution of grain size would be affected by flow

speed.

However, there were two results that were not consistent with this mechanism. The first is the iron sand distribution. The Fe_2O_3 content in the deposits in C1 and C2 showed no major decrease at x > 50 m. The Fe_2O_3 content near the inundation limit ($\approx 20\%$) was larger than that in the upper part of the inundation flow (4.4%). Because the flow speeds in C1 and C2 were lower than those in the experiments in which vertical distribution was measured, the upward decreases in C1 and C2 were steep compared with the measurements. Thus, the deposition of iron sand contradicted that predicted by the settling velocity and vertical distribution. The second contradictory result was that in C4; D_{vcs} in the onshore deposits did not change after it dropped rapidly to near 1%. If the coarse sand settled faster than the finer sand, the coarse sand should disappear near x = 55 m. Similar to D_{vcs}, the Fe_2O_3 content also showed no correlation with the distance from the shoreline.

These contradictory results could be explained by the vertical mixing in the first phase flow being strong enough to disrupt the vertical sediment distribution (Fig. 16). The first phase flows in C3 and C4 showed a rapid decrease compared with the flow expected from gravitational effects. This rapid decrease may indicate energy loss caused by the strong turbulence at the bore front. The strong mixing at the bore front can also produce a uniform vertical grain size distribution in the sediment transport.

4.2.5. Sedimentary structure of the deposits

The sediment transport measured in this study showed ordinary vertical distributions of sediment volume, grain size, and density, indicating upward thinning, fining, and decrease in density (Figs. 12 and 16). Several field studies assumed that there was a traction carpet in the sediment transport to explain the inverse grading located at the base of tsunami deposits (e.g. Moore et al., 2011). The inverse grading in the traction carpet was attributed to the grain collision in the high sediment concentration lifting large grains above the smaller ones (e.g. Sohn, 1997). If there were a traction carpet in the sediment transport, the grain size would show upward coarsening near the bed. The sediment concentration near the bottom, where D_{vcs} was dominant, reached 30% (10% by volume). At these high concentrations, the grains should collide. However, our results showed upward fining in D50 and D_{vcs}, not upward coarsening. This result casts doubt on the existence of a traction carpet in sediment transport induced by tsunamis.

The deposits near the trap showed inverse grading at the base (Figs. 13 and 16(b)). The calculated deposits did not show inverse grading; thus, the inverse grading in the deposits did not arise from the vertical grain size distribution in the sediment transport. The infiltration of fine sand into the pore space of coarse sand may create the finer bed layer; however, this process cannot explain the uplift of the coarse sand. Thus, the presence of coarse sand in the upper part of the deposits implies that the coarse sand moved during the depositional process. Based on these results, mechanisms that attribute the inverse grading to a depositional process, such as kinetic sieving (e.g. Middleton, 1970), geometrical sieving (Dasgupta and Manna, 2011), and spatial difference in flow speed (Kneller and Branney, 1995), are more plausible for explaining inverse grading in tsunami deposits.

Because the formation of inverse grading was not recorded clearly in the video images, we cannot judge which process was most plausible. We are investigating detailed sedimentary structures in an ongoing study, which will supply information about the erosional and depositional processes.

4.2.6. Sources of deposits

The sediment source is crucial in establishing the identification criteria for tsunami deposits based on shell fragments, diatoms, and other materials. Our experiments showed that the amount of sediment from the offshore region was smaller than that from the dune erosion and scouring behind the dune because the horizontal velocity in front of the dune decreased immediately after the wave reflection

(Supplementary information B.1). Recent field and numerical studies have also drawn the same conclusion. Szczuciński et al. (2012) found that on the Sendai Plain, which has a 3-m-high sand dune at the shoreline, only a very small marine sediment component was transported onshore by the 2011 Tohoku-oki earthquake tsunami based on the diatom assemblages in the deposits. Sugawara and Goto (2012) conducted numerical experiments for the same site and found that the reflection of the wave may have resulted in the accretion of a considerable amount of sediment on the beach face.

The offshore deposits contained 24% of sediment from the inundation flow. Because the experimental case with a larger wave underestimated the return flow owing to the overflow at the end of channel, the actual percentage would be larger than this estimate. Some of the onshore sediment was entrained in the seaward sediment transport because the onshore sediment mixed with sediment from scouring behind the dune. However, the amount of sediment brought back offshore was consistent with that of the dune erosion during the inundation; thus, the major source of seaward sediment transport was the dune.

These results showed that the applicability of deposit identification based on marine or land species can depend on nearshore topography. The lack of marine sediment in the onshore deposits indicated that these identification techniques are unlikely to be effective on topography with dunes, as observed by Szczuciński et al. (2012). Submarine deposits can contain species originating from the land, even for topographies with dunes, because the sediment originating from land accounts for no more than 30% of the offshore deposits. Dunes separate marine and onshore sediment by preventing inundation and return flow, and these identification techniques may more effective on a uniform sloping topography.

Because the topography and incident waves affect the sediment source ratio, we need to gather more data on different topographies and waves for quantitative evaluation. Moreover, the behavior of fine materials may differ from that of sand and their low settling velocity may allow them to be entrained in the second phase flow. Therefore, the effect of particle size on sediment source should be investigated further.

4.2.7. Offshore tsunami deposits

Our experiments provide an overview of the spatial distributions of offshore deposits not available from field studies. The offshore deposits showed seaward thinning and fining from the most eroded point regardless of the presence of the dune. The majority of offshore deposits arose from the wave motion, because the sediment supply from the onshore region accounted for < 30% of the offshore deposits. Thus, the sediment supply from the onshore region was not the main factor in the formation of offshore deposits.

The seaward thinning and fining trend disappeared when we blocked the return flow. This result strongly suggests that spatial distributions of deposition and grain size arose from the horizontal advection. Because the sediment supply from the onshore region was not significant, these sedimentary structures were caused by the seaward return flow reworking the sediment. Therefore, the return flow plays a crucial role not in sediment supply but in construction of sedimentary structures.

There are few studies of offshore tsunami deposits in field compared with the vast number of studies of onshore deposits (e.g. Haraguchi et al., 2013; Ikehara et al., 2014; Tamura et al., 2015; Yoshikawa et al., 2015). Although the offshore deposits do not suffer from artificial posttsunami alteration, the reworking caused by the post-tsunami waves can make it difficult to identify tsunami deposits, especially in the nearshore region (Tamura et al., 2015). Yoshikawa et al. (2015) used a seismic survey technique to demonstrate that the offshore deposits caused by the 2011 Tohoku-oki tsunami showed a seaward thinning trend.

Our experiments reproduced a typical characteristic of offshore deposits; however, it is only one aspect of these deposits. Because the

return flow can change the sedimentary structures of the offshore deposits, the land slope should affect the characteristics of the offshore deposits. In addition, the seabed slope should change the erosion and deposition distributions. Therefore, further investigation of the topography with different slopes in field studies, and in laboratory and numerical experiments are needed to improve our understanding of offshore tsunami deposits.

4.3. Reconstruction of tsunami hydraulic parameters

The onshore deposits could be divided into two areas reflecting the dominant flow phases that induced the deposits and each flow phase was governed by the wave parameters at specific times and places (Fig. 15 (d)). Thus, there was no direct relationship between the substantial erosion and deposition near the dune caused by the second phase flow and the inundation limit determined by the initial phase flow. Therefore, it was impossible to measure hydraulic parameters beyond these governing parameters without assuming the waveform.

If the inundation limit is determined by the initial phase flow, as observed in this study, the only way to reconstruct the inundation limit (height) is to investigate the deposits near the limit. These deposits should contain information about the inundation speed of the water mass that reached the limit. However, this approach would encounter the paradoxical problem that we would have to know that the deposits used for reconstruction are the deposits formed near the inundation limit. Therefore, a better way would be to investigate the limit of deposits, as has been attempted in many studies of ancient tsunamis (e.g. Shishikura et al., 2007; Sawai et al., 2007). Thus, the rapid change in grain size and mineral composition observed near the inundation limit in this study and field studies (e.g. Goto et al., 2011; Chagué-Goff et al., 2012a) is an important criterion for identifying deposits near the limit.

The deposits from the return flow, which formed the upper part of nearshore deposits, can contain sediment carried by the initial phase flow (Fig. 15 (d)). These deposits could be used to estimate the inundation limit. For example, because the speed of return flow is determined by the distance from the inundation limit and the land slope, the amount of deposits carried by the return flow should reflect how far the inundation flow reached. However, interpreting the deposits caused by the return flow would be more complex owing to sediment from different phase flows mixing.

The deposits from the second phase flow would enable us to estimate the wave level in front of the dune (Fig. 15 (b-1)). This nearshore deposit could be sufficiently thick to observe sedimentary structures. Theoretical inverse analysis of deposits has been used to estimate the flow speed caused by the inundation flow (e.g. Jaffe and Gelfenbuam, 2007; Spiske et al., 2010; Jaffe et al., 2011, 2012). The water depth and flow velocity estimated from the inverse analysis would eventually give the water level in front of the dune. This information is not related directly to the onshore maximum inundation depth, but would contribute to estimating the maximum tsunami height around the shoreline.

The simplest and most robust method for reconstructing the inundation depth may be to obtain information about offshore erosion, especially near dunes. Because the seaward current over dunes is determined by the difference in water levels in front of and behind the dune, the erosion in front of the dune should reflect the inundation depth behind the dune. In particular, the maximum depth and the shape of scouring are expected to reflect the offshore current over the dune. Moreover, the substantial deposition that fills eroded areas would protect the erosion surface from post-tsunami erosion from storm waves and surges. The greatest advantage in using erosion information is that the complicated and poorly understood process of sediment transport does not need to be considered. Currently, it is difficult to assess whether this approach is feasible in the field owing to inadequate field research on offshore deposition and erosion distribution. The spatial distribution of the bottom of the offshore deposits has been

demonstrated by using the seismic survey technique (Yoshikawa et al., 2015); thus, it may be technically possible to investigate offshore scouring. In addition to field investigations, further experimental and numerical investigations are needed to underpin this approach.

5. Conclusion

Large-scale experiments, which were conducted as part of the TSTLE project, enabled us to investigate the processes of tsunami propagation, inundation, sediment transport, and subsequent deposits on topography with a 1/50 slope at Shields numbers of up to 8. The inundation process on topography with a dune was categorized into first and second phase flows. The first phase flow was governed by the wave speed at the shoreline and the land slope, whereas the second phase flow was governed by the difference in water level at the dune.

The vertical distribution of grain size and density in the inundation flow showed upward fining and upward lightening, and there was no evidence of a traction carpet. The deposits showed inverse grading at the base in addition to normal grading, and they showed landward thinning and fining and seaward thinning and fining from the place where erosion reached its maximum. Furthermore, the deposits near the limit showed a rapid change in grain size and chemical component, which was attributed to the sediment carried in the muddy foam on the water surface.

The sediment from the dune was estimated to reach up to 36% of the onshore deposits, and there was little sediment from offshore. In contrast, 32% and 24% of offshore deposits were estimated to have come from the dune and the onshore region, respectively. We confirmed that the offshore deposits formed without the return flow, although the return flow substantially affected the formation of sedimentary structures, such as seaward thinning and fining.

The understanding of deposits obtained in this study will contribute considerably to the interpretation of tsunami deposits in the field. An overall understanding of sediment transport and deposition will help establish the physical background that exemplifies the empirically developed identification criteria for tsunami deposits. Moreover, the detailed data set of hydraulic and sedimentary characteristics obtained in this study can be used to evaluate the accuracy and physical basis of numerical simulations. To generalize the sediment transport, topography change, and sedimentary structures observed in this study, further studies using different topography and incident waves are needed.

Appendix A. Supplementary data

Supplementary data to this article can be found online at http://dx.doi.org/10.1016/j.margeo.2017.07.020.

References

Chagué-Goff, C.C., Andrew, A.A., Szczuciński, W.W., Goff, J.J., Nishimura, Y.Y., 2012a. Geochemical signatures up to the maximum inundation of the 2011 Tohoku-oki tsunami - implications for the 869 AD Jogan and other palaeotsunamis. Sediment. Geol. 282, 65–77.
Chagué-Goff, C.C., Goff, J.J., Nichol, S.S., Dudley, W.W., Zawadzki, A.A., Bennett, J.J., Mooney, S.S., Fierro, D.D., Heijnis, H.H., Dominey-Howes, D.D., Courtney, C.C., 2012b. Multi-proxy evidence for trans-Pacific tsunamis in the Hawai'ian Islands. Mar.

Geol. 299-302, 77–89.

Chagué-Goff, C.C., Schneider, J.J., Goff, J.J., Dominey-Howes, D.D., Strotz, L.L., 2011. Expanding the proxy toolkit to help identify past events - lessons from the 2004 Indian ocean tsunami and the 2009 South Pacific Tsunami. Earth Sci. Rev. 107 (1-2), 107–122.

Dasgupta, P.P., Manna, P.P., 2011. Geometrical mechanism of inverse grading in grain-flow deposits: an experimental revelation. Earth Sci. Rev. 104 (1-3), 186–198.

Furusato, E.E., Tanaka, N.N., 2014. Maximum sand sedimentation distance after back-wash current of tsunami - simple inverse model and laboratory experiments. Mar. Geol. 353 128–113.

Goff, J.J., Nichol, S.S., Kennedy, D.D., 2010. Development of a palaeotsunami database for New Zealand. Nat. Hazards 54 (2), 193–208.

González, F.F., Bernard, E.E., Dunbar, P.P., Geist, E.E., Jaffe, B.B., Kânoğlu, U.U., Locat, J.J., Mofjeld, H.H., Moore, A.A., Synolakis, C.C., Titov, V.V., Weiss, R.R., 2007. Scientific and technical issues in tsunami hazard assessment of nuclear power plant sites. Tech. Rep. NOAA Tech. Memo. OAR PMEL-136. Pacific Marine Environmental Laboratory, Seattle, WA.

Goto, K.K., Chagué-Goff, C.C., Fujino, S.S., Goff, J.J., Jaffe, B.B., Nishimura, Y.Y., Richmond, B.B., Sugawara, D.D., Szczuciński, W.W., Tappin, D.D., Witter, R.R., Yulianto, E.E., 2011. New insights of tsunami hazard from the 2011 Tohoku-oki event. Mar. Geol. 290 (1-4), 46–50.

Goto, K.K., Hashimoto, K.K., Sugawara, D.D., Yanagisawa, H.H., Abe, T.T., 2014. Spatial thickness variability of the 2011 Tohoku-oki tsunami deposits along the coastline of Sendai Bay. Mar. Geol. 358, 38–48.

Gusman, A.R.A.R., Tanioka, Y.Y., Takahashi, T.T., 2012. Numerical experiment and a case study of sediment transport simulation of the 2004 Indian Ocean tsunami in Lhok Nga, Banda Aceh, Indonesia. Earth Planets Space 64 (10), 3.

Harada, K.K., Imai, K.K., Tran, T.A.T.A., Fujiki, Y.Y., 2011. Hydraulic experiment on sand deposit by tsunami run-up with land slope. J. JSCE, Ser. B2 (Coast. Eng.) 67 (2), 252–255 (in Japanese with an English abstract).

Haraguchi, T.T., Goto, K.K., Sato, M.M., Yoshinaga, Y.Y., Yamaguchi, N.N., Takahashi, T.T., 2013. Large bedform generated by the 2011 Tohoku-oki tsunami at Kesennuma Bay, Japan. Mar. Geol. 335, 200–205.

Honma, H.H., 1940. Coefficient of flow volume on low overflow weir. Civ. Eng. JSCE 26 (6), 635–645 (in Japanese).

Ikehara, K.K., Irino, T.T., Usami, K.K., Jenkins, R.R., Omura, A.A., Ashi, J.J., 2014. Possible submarine tsunami deposits on the outer shelf of Sendai Bay, Japan resulting from the 2011 earthquake and tsunami off the Pacific coast of Tohoku. Mar. Geol. 358, 120–127.

Jaffe, B.B., Buckley, M.M., Richmond, B.B., Strotz, L.L., Etienne, S.S., Clark, K.K., Watt, S.S., Gelfenbaum, G.G., Goff, J.J., 2011. Flow speed estimated by inverse modeling of sandy sediment deposited by the 29 September 2009 tsunami near Satitoa, East Upolu, Samoa. Earth Sci. Rev. 107 (1), 23–37.

Jaffe, B.B., Gelfenbuam, G.G., 2007. A simple model for calculating tsunami flow speed from tsunami deposits. Sediment. Geol. 200 (3), 347–361.

Jaffe, B.B., Goto, K.K., Sugawara, D.D., Gelfenbaum, G.G., La, S.S., 2016. Uncertainty in tsunami sediment transport modeling. J. Disaster Res. 11 (4), 647–661.

Jaffe, B.B., Goto, K.K., Sugawara, D.D., Richmond, B.B., Fujino, S.S., Nishimura, Y.Y., 2012. Flow speed estimated by inverse modeling of sandy tsunami deposits: results from the 11 March 2011 tsunami on the coastal plain near the Sendai Airport, Honshu, Japan. Sediment. Geol. 282, 90–109.

Japan Nuclear Energy Safety Organization, 2014. Guideline for tsunami deposit survey and evaluation. JNES-RE-Report Series. Japan Nuclear Energy Safety Organization.

Johnson, J.J., Delbecq, K.K., Kim, W.W., Mohrig, D.D., 2016. Experimental tsunami deposits: linking hydrodynamics to sediment entrainment, advection lengths and downstream fining. Geomorphology 253, 478–490.

Kneller, B.B., Branney, M.M., 1995. Sustained high-density turbidity currents and the deposition of thick massive sands. Sedimentology 42 (4), 607–616.

Middleton, G.V.G.V., 1970. Experimental Studies Related to Problems of Flysch Sedimentation. Geological Association of Canada.

Monecke, K.K., Finger, W.W., Klarer, D.D., Kongko, W.W., McAdoo, B.B., Moore, A.A., Sudrajat, S.S., 2008. A 1,000-year sediment record of tsunami recurrence in Northern Sumatra. Nature 455 (7217), 1232–1234.

Moore, A.A., Goff, J.J., McAdoo, B.B., Fritz, H.H., Gusman, A.A., Kalligeris, N.N., Kalsum, K.K., Susanto, A.A., Suteja, D.D., Synolakis, C.C., 2011. Sedimentary deposits from the 17 July 2006 Western Java tsunami, Indonesia: use of grain size analyses to assess tsunami flow depth, speed, and traction carpet characteristics. Pure Appl. Geophys. 168 (11), 1951–1961.

Namegaya, Y.Y., Satake, K.K., 2014. Reexamination of the A.D. 869 Jogan earthquake size from tsunami deposit distribution, simulated flow depth, and velocity. Geophys. Res. Lett. 41 (7) 2013GL058678.

Nanayama, F.F., Satake, K.K., Furukawa, R.R., Shimokawa, K.K., Atwater, B.B., Shigeno, K.K., Yamaki, S.S., 2003. Unusually large earthquakes inferred from tsunami deposits along the Kuril trench. Nature 424 (6949), 660–663.

Peters, R.R., Jaffe, B.B., 2010. Identification of tsunami deposits in the geologic record: developing criteria using recent tsunami deposits. U.S. Geological Survey Open-File Report 2010-1239. 39.

Prendergast, A.A., Cupper, M.M., Jankaew, K.K., Sawai, Y.Y., 2012. Indian Ocean tsunami recurrence from optical dating of tsunami sand sheets in Thailand. Mar. Geol. 295-298, 20–27.

Sawai, Y.Y., Shishikura, M.M., Okamura, Y.Y., Takada, K.K., Matsu'ura, T.T., Aung, T.T.T.T., Kamataki, T.T., Sato, N.N., 2007. A study of paleotsunami using handy geoslicer in Sendai Plain (Sendai, Natori, Iwanuma, Watari, and Yamamoto), Miyagi, Japan. Annu. Rep. Active Fault Paleoearthquake Res. 7, 47–80 (in Japanese with an English abstract).

Shen, M.C.M.C., Meyer, R.E.R.E., 1963. Climb of a bore on a beach. Part 3. Run-up. J. Fluid Mech. 16, 113–125.

Shishikura, M.M., Sawai, Y.Y., Okamura, Y.Y., Komatsubara, J.J., Aung, T.T.T.T., Ishiyama, T.T., Fujiwara, O.O., Fujino, S.S., 2007. Age and distribution of tsunami deposit in the Ishinomaki Plain, Northeastern Japan. Annu. Rep. Active Fault Paleoearthquake Res. 7, 31–46 (in Japanese with an English abstract).

Sohn, Y.Y., 1997. On traction-carpet sedimentation. J. Sediment. Res. 67 (3), 502–509.

Soulsby, R.R., Smith, D.D., Ruffman, A.A., 2007. Reconstructing tsunami run-up from sedimentary characteristics - a simple mathematical model. In: 6th International Symposium on Coastal Engineering and Science of Coastal Sediment Process, pp. 1075–1088.

Spiske, M.M., Weiss, R.R., Bahlburg, H.H., Roskosch, J.J., Amijaya, H.H., 2010. The TsuSedMod inversion model applied to the deposits of the 2004 Sumatra and 2006 Java tsunami and implications for estimating flow parameters of palaeo-tsunami. Sediment. Geol. 224 (1), 29–37.

Sugawara, D.D., Goto, K.K., 2012. Numerical modeling of the 2011 Tohoku-oki tsunami in the offshore and onshore of Sendai Plain, Japan. Sediment. Geol. 282, 110–123.

Sugawara, D.D., Takahashi, T.T., Imamura, F.F., 2014. Sediment transport due to the 2011 Tohoku-oki tsunami at Sendai: results from numerical modeling. Mar. Geol. 358, 18–37.

Szczuciński, W.W., Kokociński, M.M., Rzeszewski, M.M., Chagué-Goff, C.C., Cachão, M.M., Goto, K.K., Sugawara, D.D., 2012. Sediment sources and sedimentation processes of 2011 Tohoku-oki tsunami deposits on the Sendai Plain, Japan - insights from diatoms, nannoliths and grain size distribution. Sediment. Geol. 282, 40–56.

Takahashi, T.T., Shuto, N.N., Imamura, F.F., Asai, D.D., 2000. Modeling sediment transport due to tsunamis with exchange rate between bed load layer and suspended load layer. In: Proceedings of the International Conference on Coastal Engineering. vol. 276. pp. 1508–1519.

Tamura, T.T., Sawai, Y.Y., Ikehara, K.K., Nakashima, R.R., Hara, J.J., Kanai, Y.Y., 2015. Shallow-marine deposits associated with the 2011 Tohoku-oki tsunami in Sendai Bay, Japan. J. Quat. Sci. 30 (4), 293–297.

Tang, H.H., Weiss, R.R., 2015. A model for tsunami flow inversion from deposits (TSUFLIND). Mar. Geol. 370, 55–62.

Yamaguchi, N.N., Sekiguchi, T.T., 2015. Effects of tsunami magnitude and terrestrial topography on sedimentary processes and distribution of tsunami deposits in flume experiments. Sediment. Geol. 328, 115–121.

Yoshii, T.T., Ikeno, M.M., Matsuyama, M.M., 2009. Experimental study of sediment transport caused by tsunami. In: Proceedings of Coastal Dynamics 2009, pp. 1–11.

Yoshii, T.T., Ikeno, M.M., Matsuyama, M.M., Fujii, N.N., 2011. Pick-up rate of suspended sand due to tsunami. In: Proceedings of International Conference of Coastal Engineering 2010, pp. 1–15.

Yoshikawa, S.S., Kanamatsu, T.T., Goto, K.K., Sakamoto, I.I., Yagi, M.M., Fujimaki, M.M., Imura, R.R., Nemoto, K.K., Sakaguchi, H.H., 2015. Evidence for erosion and deposition by the 2011 Tohoku-oki tsunami on the nearshore shelf of Sendai Bay, Japan. Geo-Mar. Lett. 35 (4), 315–328.

Further reading

Iwagaki, Y.Y., 1956. Fundamental study on critical tractive force: (1) hydrodynamical study on critical tractive force. Trans. Jpn Soc. Civ. Eng. 41, 1–21.